RSC Applied Interfaces

ROYAL SOCIETY OF CHEMISTRY

PAPER

View Article Online
View Journal | View Issue

Cite this: *RSC Appl. Interfaces*, 2024, 1, 591

The effects of selectively blocking the electron transport layer of n-i-p perovskite solar cells with polymer particles on device performance†

Amal Altujjar, *[ab] Ran Wang, [a] Xuelian Wang,[a] Jennifer M. Saunders,[a] Zhenyu Jia, [a] Ben Spencer, [ac] Nigel Hodson,[d] Janet Jacobs,[c] Osama M. Alkhudhari, [a] Andrew Thomas,[ac] Richard Curry [ce] and Brian R. Saunders *[a]

Perovskite solar cells (PSCs) continue to attract considerable academic and industrial interest due to their excellent potential to contribute to solar energy generation. The application of PSCs will benefit from improvements in the understanding of the roles of the interfaces present in charge transport and recombination. The buried perovskite/electron transport layer (ETL) interface in n-i-p PSCs is relatively difficult to study, particularly when molecular additives are used to target that region because they are not able to be visualized by electron microscopy. Here, we use sub-micrometer insulating polystyrene microgel particles (PS MGs) to partially cover the ETL of PSCs. The MGs provide well-defined colloidal additives for selectively covering the ETL because they are laterally constrained and the coverage is readily tuneable. We examine the effect of MG concentration on the device performance and find that the MGs passivate the SnO_2 ETL and obstruct charge transport. We then engineer gaps between the deposited MGs using UV/ozone treatment and achieve a maximum power conversion efficiency (PCE) of 20.09% compared to 19.60% for the control. Remarkably, the PSCs can still function efficiently even when the ETL is mostly covered by the MGs. We show that the most efficient devices have partially covered ETLs with a lateral blocking distance of ~500 nm. This work demonstrates that mostly covering the ETL with insulating particles does not necessarily lead to a catastrophic decrease in performance. In contrast, this study provides a new scalable method for improving the PCE and for potentially enhancing light management for PSCs in the future.

Received 23rd February 2024,
Accepted 13th March 2024

DOI: 10.1039/d4lf00062e

rsc.li/RSCApplInter

Introduction

Perovskite solar cells (PSCs) remain the most exciting development in solar cell research[1–8] in the last 15 years.[9] The understanding of charge transport and recombination within the devices has become mature.[4,10,11] However, the buried interface of n-i-p devices has received relatively less attention than the other parts of the device[12] because it is difficult to study. The effects of additives deposited on the electron transport layer (ETL) of PSCs are a relatively underexplored area.[12–15] Ionic molecules[16–20] and nanomaterials[21–23] have been used as passivation layers at the SnO_2/perovskite interface to suppress ion migration and enhance carrier lifetimes. Chemical modification of the buried ETL/perovskite interface using isobutylammonium chloride improved charge extraction.[14] DL-carnitine hydrochloride has been used as a passivation layer at the SnO_2/perovskite interface to passivate the oxygen vacancies and Sn-related defects.[15] Indeed, a number of recent studies have reported that defects associated with SnO_2 (ref. 24) require surface treatments and/or the use of additives to improve PSC performance.[15,25–28] Whilst the above studies have provided important information about the buried interface, selectively blocking regions of the ETL in a well-defined manner and studying the effects of such blocking on PSC performance have only rarely been reported.[29] Here, we investigate the effects of partially covering the SnO_2 ETL of n-i-p PSCs with well-defined polymer blocking species on device performance.

[a] *Department of Materials, University of Manchester, MECD, Building A, Manchester, M1 7HL, UK. E-mail: brian.saunders@manchester.ac.uk*
[b] *Basic Science Department, Deanship of Preparatory Year and Supporting Studies, Imam Abdulrahman Bin Faisal University, Dammam 34221, Kingdom of Saudi Arabia. E-mail: araltujjar@iau.edu.sa*
[c] *Photon Science Institute and The Henry Royce Institute, University of Manchester, Manchester, M13 9PL, UK*
[d] *BioAFM Facility, Faculty of Biology, Medicine and Health, Stopford Building, University of Manchester, Oxford Road, Manchester, M13 9PT, UK*
[e] *Department of Electrical and Electronic Engineering, University of Manchester, Manchester M13 9PL, UK*

† Electronic supplementary information (ESI) available. See DOI: https://doi.org/10.1039/d4lf00062e

In this study, we use polystyrene microgel particles (PS MGs) as the building blocks to partially cover the ETL. Microgels are crosslinked polymer colloid particles that swell in a good solvent.[30] There are only a few reports that use conventional (non-microgel) PS at the ETL/perovskite interface.[31–33] For example, linear PS was deposited as an interlayer between perovskite and the hole transport layer (HTL)[32,34–38] and was effective in passivating perovskite defects.[32,35,39] The efficiency of semitransparent PSCs containing a perovskite island morphology was improved by coating the TiO_2/perovskite interface[31] with PS as a passivation layer. The PS used to date in PSCs has been in the form of deposited ultrathin films[31,32,35,39] that are difficult to directly visualize using microscopy techniques and the thickness values have not been reported. The PS films were likely too thin to be visualized or measured. This inevitably results in a degree of ambiguity regarding the interpretation of their role in affecting charge carrier transport. Here, we use sub-micrometer size PS MGs that are readily imaged to improve the understanding of how partial blocking of the ETL with an insulator impacts n-i-p PSC performance.

Microgels are intrinsically solute tolerant when dispersed in a good solvent. Hence, they have outstanding colloidal stability in dispersed solutions and during deposition that enables them to be readily introduced into different regions of PSCs whilst improving device performance.[40,41] We previously used poly(*N*-isopropylacrylamide) microgels as sacrificial templates to control the porosity within the *meso*-TiO_2 layer of mesoporous PSCs.[42] We also blended PS MGs with conjugated polymers and deposited composite hole transport layers (HTLs) within PSCs.[43] The present study differs greatly from our previous work because here we focus on PS MGs deposited at the buried ETL/perovskite interface of PSCs for the first time. Our approach depicted in Fig. 1 enables us to define the blocking area of the buried interface as well as the blocking distance. This unique approach enables testing of two hypotheses in this work. (1) Partial blocking of the ETL of an n-i-p PSC by PS polymer particles would decrease recombination *via* passivation and increase the PCE. (2) If the blocking distance is less than the photoexcited charge diffusion length, then the PSC with a partially blocked ETL can function efficiently.

Our strategy in this study is to partially coat the ETL with well-defined insulating PS MGs that are easily visible by electron microscopy so that the coverage can be easily measured. The perovskite layer was then spin-coated on the ETL/PS MG layer and PSCs constructed (Fig. 1). We then study the effects of ETL coverage on PSC performance. We verify that MGs remain at the buried interface after the deposition of the perovskite layer and show that the PS MGs passivate the ETL. We report that if the distance blocked by MGs is less than the charge diffusion length, then the photogenerated electrons can reach the ETL and be transferred to the external circuit (labelled process (ii) in Fig. 1). The results show that the open circuit voltage (V_{oc}) increases when the ETL is partially covered by the insulating PS MGs. Remarkably, relatively high PCEs and short-circuit current densities (J_{sc}) are found even when most of the ETL is blocked by the particles. Using UV/ozone (UVO) treatment, we open up gaps between neighboring MGs, which enables a best PCE of 20.09% compared to the control PCE of 19.60%. We conclude that partially coating an ETL with separated insulating particles is beneficial for PSC performance. PS MG preparation is scalable and the MGs are easily deposited to selectively block the ETL of PSCs. Furthermore, in principle the lateral blocking distance can be tuned using UVO. Hence, our lateral blocking approach for ETLs using PS MGs should be able to provide passivation at the buried interface and performance improvements for other PSCs.

Results and discussion

Characterization of electron transport layers coated with PS MGs

An amine functionalized initiator (2,2′-azobis(2-methylpropionamidine)dihydrochloride) was used to prepare the PS MGs in this study because initiator fragments bond to PS chain ends (Fig. 1) and amine groups bind to perovskite. Zeta potential data (later) confirmed that the as-made MGs

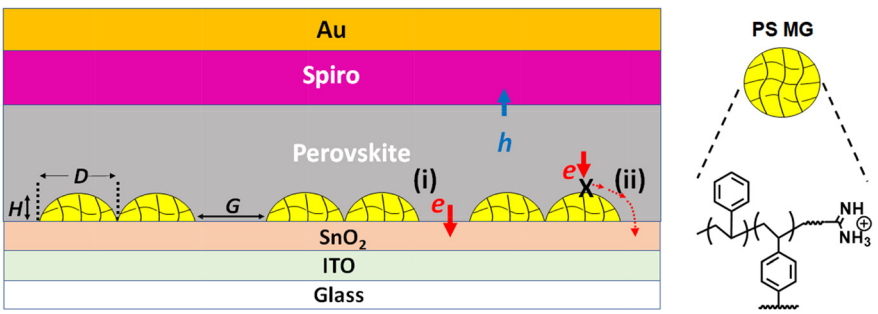

Fig. 1 Schematic illustration of charge transport in PSCs employed in this study with an n-i-p architecture containing PS MG particles at the SnO_2/perovskite interface. The electron and hole charge carriers are represented by e and h, respectively. The particle height and diameter are represented by *H* and *D*, respectively. *G* shows the gap distance between particles. Labels (i) and (ii) show the direct and lateral transfer of electrons from the perovskite layer to the SnO_2, respectively.

are cationic when dispersed in water due to the amine groups. The PS MGs were prepared in water (a non-solvent for PS) using emulsion polymerization and then transferred to chlorobenzene (CBZ, a good solvent for PS). SEM data (Fig. S1, ESI†) show that the average diameter of the MGs deposited from water and CBZ is 445 ± 23 nm and 912 ± 80 nm, respectively. The size differences of the deposited MGs show that they were, indeed, swollen in CBZ prior to deposition. A representative AFM image and a line profile (Fig. 2A) show that the MGs flattened when deposited from CBZ. The particle diameter and height are ~1100 nm and ~120 nm, respectively. The aspect ratio (diameter/height) is 9.2 which shows that the MGs flatten considerably, which is expected when microgels are deposited from a good solvent.[44]

We noticed that PS MGs deposited on the ETL substrate (glass/ITO/SnO_2) tended to pack closely together as the solvent evaporated, which is due to surface tension (Fig. S2, ESI†). The peripheries of the MGs interpenetrate which is the basis for film formation of such particles in surface coatings. The closely packed MGs form "islands". However, gaps appear between neighboring particles due to packing errors. These gaps become deeper when the particles are spaced further apart. The MGs were spin-coated onto the glass/ITO/SnO_2 substrates and examined using SEM. The size of the hexagonally close-packed MG islands increases (Fig. 2B and S3 (ESI†)) and the space between the MG islands decreases as the MG concentration used increases. We calculated the coverage of the ETL by measuring the fraction of the ETL area covered by the MGs (Fig. 2C, cartoon) *via* ImageJ. The coverage increases with increasing MG concentration (Fig. 2C) reaching 85.2% at 20 mg mL^{-1}. Contact angle data showed that the substrate changed from hydrophilic (4.2°) to hydrophobic (87.6°) as the MG concentration increased from 0 to 20 mg mL^{-1} (Fig. S4, ESI†), which confirms that coverage occurred.

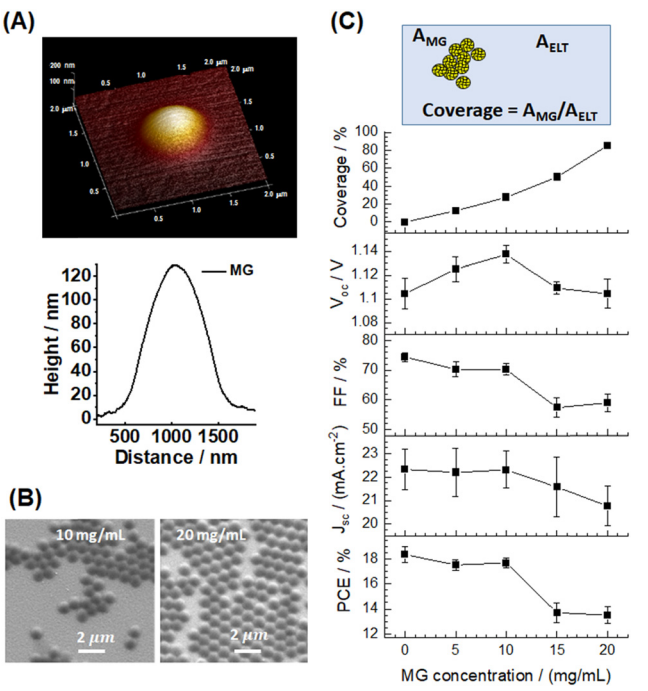

Fig. 2 (A) A 3D AFM perspective image and a line profile for a representative MG particle. (B) SEM images of MGs deposited on glass/ITO/SnO_2 using two concentrations. (C) Coverage and PSC performance parameter variation with MG concentration used. A_{MG} and A_{ETL} are the total areas of the MGs and ETL.

Verifying that the MGs remain on the ETL after perovskite film deposition

Having deposited the MGs onto the ETLs, it was essential to verify that the MGs remained on the ETL after the deposition of the perovskite films. We first consider the morphology of the perovskite layer. SEM images show that the top surface perovskite morphology and grain size are not significantly affected by the MG coverage (Fig. S5A–C, ESI†). The average grain size is in the range of 370–405 nm (Fig. S5D, ESI†). We then washed away the perovskite film deposited on top of these particles with water (a good solvent for perovskite but a bad solvent for PS) and re-examined the ETL surface (Fig. S6, ESI†). The PS MGs remained and no change in coverage was detected. To confirm that the MGs were not detached during perovskite deposition, we obtained SEM cross-sections of the perovskite films (Fig. S7, ESI†). The film thickness was 430–530 nm and was largest for the MG systems. Importantly, MGs are readily identified on the buried ETL surface. Hence, the MGs are not removed after being deposited on glass/ITO/SnO_2 as a result of subsequent perovskite precursor spin-coating and perovskite crystallization.

Performance of glass/ITO/SnO_2/MG-based perovskite devices

We constructed devices (Fig. 1) and investigated the effects of MG concentration on their performance (Fig. 2C and Table S1 (ESI†)). The V_{oc} values increase at first reaching a maximum of 1.14 V when the MG concentration is 10 mg mL^{-1} before decreasing at higher concentrations (Fig. 2C and S8A (ESI†)). An increase in V_{oc} indicates that fewer defects are present when the MGs partially cover the ETL/perovskite interface. The fill factor (FF) decreases slightly at first and then more rapidly at MG concentrations of 15 and 20 mg mL^{-1} (Fig. 2C and S8B (ESI†)). The J_{sc} values are constant up until a concentration of 10 mg mL^{-1} and then decrease gradually for 15 and 20 mg mL^{-1} (Fig. 2C and S8C (ESI†)). The PCE decreases from the best value for the control of 19.60% to 18.43% for the 10 mg mL^{-1} MG system, and decreases further to 14.68% and 14.15%, respectively, for the 15 and 20 mg mL^{-1} MG systems (Fig. 2C and S8D, ESI†). It is remarkable that the 20 mg mL^{-1} MG-based device still functioned with an ETL coverage of 85.2%. This is largely due to the appreciable J_{sc} value (>20 mA cm^{-2}) (Fig. 2C) and this is discussed further below. EQE data (Fig. S9, ESI†) confirm the accuracy of the J_{sc} values. The hysteresis index decreased from 12.58% for the control to 1.19% for the 20 mg mL^{-1} system as the MG concentration increased (Table

S1, ESI†) indicating much less build-up of mobile ions at the ETL/perovskite interface covered by MGs. Analysis of these data shows that the PCE changes for these devices are dominated by the FF values because a plot of PCE *vs.* FF gives a strongly linear relationship (Fig. S10, ESI†).

To probe defect densities, SCLC measurements were performed using electron-only devices (Fig. S11, ESI†). The data enabled calculation of the number density of defects (N_d) using[45]

$$N_d = \frac{2\varepsilon\varepsilon_0 V_{TFL}}{qL^2} \quad (1)$$

where ε and ε_0 are the relative dielectric constant for perovskite (46.9)[45] and the vacuum dielectric constant, respectively. L is the perovskite film thickness which is taken from Fig. S7D (ESI†). The calculated N_d value for the 10 mg mL^{-1} system (5.7×10^{15} cm^{-3}) is lower than that for the control (6.8×10^{15} cm^{-3}). The calculated N_d for the 20 mg mL^{-1} system is 6.2×10^{15} cm^{-3}, which is also lower than the control. Hence, these data indicate passivation of the perovskite.

Why ETLs that are more than 50% covered by PS MGs provide significant PCE values

The best PCE values for the 15 and 20 mg mL^{-1} MG-based devices (14.68% and 14.15%, respectively) are remarkably high given the high ETL coverages (50.2% and 85.2%, respectively). These relatively high PCEs are enabled by the relatively high J_{sc} values (Fig. 2C). However, it is important to note that the J_{sc} values are approximately constant until the coverage of the ETL reaches 30%, after which J_{sc} decreases (see Fig. S12, ESI†). Hence, the MGs do not facilitate charge transport. Importantly, they do not obstruct charge transport significantly until the coverage exceeds 30%. A key question concerns how ETLs that are mostly covered by insulating PS particles provide J_{sc} values that are more than 90% of the J_{sc} value for the MG-free control system. As gaps between MGs become larger the depth of such gaps must increase. This implies that inter-MG gaps may provide facile transport pathways for photogenerated electrons to the ETL. The diffusional distance of photogenerated charge carriers in perovskite is ~1 μm.[8,46] If a gap between MG particles is within a distance of 1 μm from where an exciton is created, then the photogenerated electrons can transfer to the ETL. Expanded view SEM images for the ETLs covered with MGs deposited at concentrations of 15 and 20 mg mL^{-1} (Fig. S13, ESI†) show that the hexagonal close-packed MG islands have many packing errors that provide inter-MG gaps. Hence, the ability to provide reasonably high J_{sc} values in the 15 and 20 mg mL^{-1} PSCs despite the high coverages is attributed to the presence of many MG packing errors within the MG close-packed islands that allow a high proportion of photogenerated electrons to reach the ETL.

Passivation in perovskite films on ETLs partially covered with MGs

Steady-state and time-resolved PL measurements were conducted to probe the photogenerated charge lifetimes. The steady-state PL data (Fig. 3A) have two contributions that reduce the observed intensity: quenching from photogenerated electrons moving to the ETL and also non-radiative recombination. The PL intensity increases with MG concentration (Fig. 3A and B) which is consistent with less quenching at the ETL as well as decreased non-radiative recombination. The latter implies increased passivation.[35] To assess the contribution of quenching to these data, we

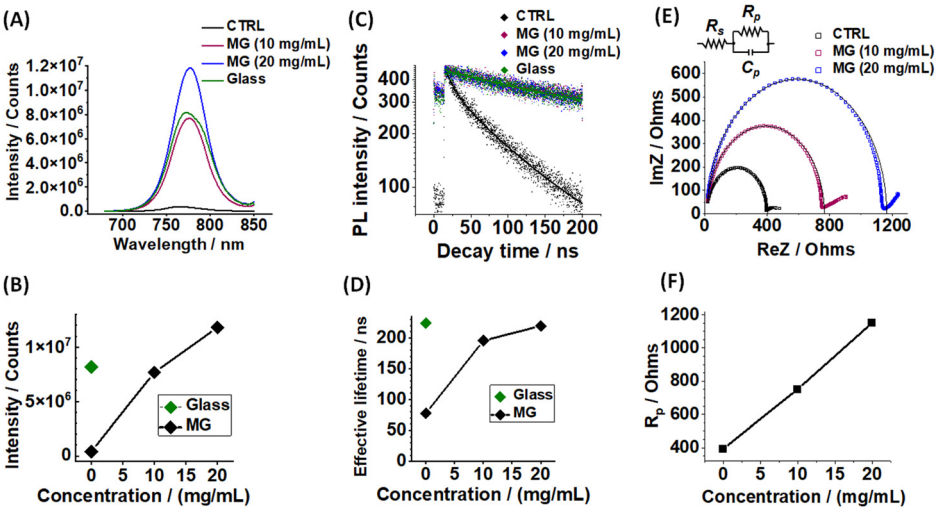

Fig. 3 (A) Steady state PL spectra for the perovskite films deposited on glass/ITO/SnO_2 substrates partially covered by MGs. (B) PL intensity from the spectra shown in (A) as a function of MG concentration. (C) TRPL data for the films. (D) Effective lifetime for systems shown in (C). Data for the perovskite film deposited on glass are also included. (E) Nyquist plots for the impedance data and a depiction of the circuit model used to fit the data. (F) The parallel resistance (R_p) as a function of MG concentration from the fits shown in (E).

employed glass as a substrate to prevent charge transfer. The high PL intensity for perovskite deposited on glass (Fig. 3A and B) indicates that quenching was a major contribution to the very low PL intensity for the MG-free control system.

TRPL data were also measured (Fig. 3C) and fitted using[47]

$$I_{PL} = A\exp\left(-\frac{t}{\tau_{fast}}\right) + B\exp\left(-\frac{t}{\tau_{slow}}\right) \quad (2)$$

where A and B are the amplitudes. The parameters τ_{fast} and τ_{slow} characterize surface and bulk recombination, respectively.[48] They are combined to provide the amplitude-weighted effective photogenerated charge lifetime (τ_{eff}) using the following equation.[47]

$$\tau_{eff} = \frac{A\tau_{fast} + B\tau_{slow}}{A + B} \quad (3)$$

All the parameters from fitting the TRPL data are shown in Table S2 (ESI†). The τ_{eff} values (Fig. 3D) increase with MG concentration and approach that for perovskite on glass. These data confirm that a major contribution to the changes in the lifetimes of the charge carriers is quenching due to charge transfer to the ETL and that such transfer is obstructed by the MGs.

Electrochemical impedance spectroscopy (EIS) data were measured to further probe passivation. The data are shown as Nyquist plots for the control, 10 mg mL^{-1} and 20 mg mL^{-1} MG systems (Fig. 3E). The EIS data are fitted using the Randles cell model (Fig. 3E) and the fitting parameters are given in Table S3 (ESI†). R_p is assigned to recombination at the buried interface[49,50] and C_p is the capacitance. The R_p data show that the resistance to recombination increases as the ETL is increasingly covered by the MGs (Fig. 3F). The increase in R_p indicates increasing passivation of the perovskite at the buried PS MG/perovskite interface. The series resistance (R_s) increases from 11.4 Ω to 14.8 Ω (Table S3, ESI†) as the MG concentration increases from 0 to 20 mg mL^{-1} as expected for increased coverage of the ETL by an insulator.

An important question concerns which part of the MG is responsible for the passivation effects reported above. All the results above were obtained using an amine-functionalized MG that contained residual amine groups from the initiator used for particle growth (Fig. 1). We investigated the effect of the charge state of these groups by synthesizing anionic PS MGs containing a carboxylate-containing initiator (4,4′-azobis(4-cyanovaleric acid)) as described in the Experimental details section (ESI†). We denote these carboxylate-functionalized MGs as MG-COOH. The characterization (Fig. S14, ESI†), PSC (Fig. S15, ESI†) and PL data (Fig. S16, ESI†) are discussed in Additional Note S1 (ESI†). The MG-COOH particles were negatively charged when dispersed in water at pH 6.7. They were transferred to CBZ and used to partially coat the glass/ITO/SnO_2 surface prior to perovskite film deposition and device construction. The PSC device data show that an increase in V_{oc} occurs using 10 mg mL^{-1} MG-COOH particles (Fig. S15A, ESI†) in agreement with Fig. 2C. Also, passivation is evidenced by steady-state and TRPL data (Fig. S16, ESI†) prepared using MG-COOH. Hence, the nature of the initiator used and the resulting functional groups bonded to the MGs does not govern passivation at the ETL surface. Therefore, the MG-triggered passivation is attributed to the insulating nature of these PS-based MG particles and their photogenerated charge blocking effect.

Proposed mechanism for passivation at the buried interface by microgels

Although SnO_2 is widely used as an ETL in PSCs, it has oxygen vacancies and interstitial Sn defects[24] which act as recombination centres necessitating passivation of the SnO_2 interface to improve device performance.[20,26] Our partial blocking approach for the SnO_2 ETLs used here (Fig. 1) is related to the partial coverage of nanostructured TiO_2 ETLs reported by Peng *et al.* for their PSCs.[29] They prepared nanoscale localized contacts on ETLs consisting of TiO_2 nanorods partially covered with an insulating polymer. The latter decreased the density of recombination-active defects at the TiO_2/perovskite interface. A related approach has also been used successfully to increase the performance of Si solar cells.[51] Peng *et al.* reported a trade-off between increasing V_{oc} (by decreasing interfacial recombination) and decreasing FF (by decreasing charge extraction) as the coverage increased.[29] We observe similar trends for our systems because Fig. 2C shows that V_{oc} reaches a maximum and FF decreases as the ETL coverage increases. Hence, the number density of SnO_2 defects per unit area surface of the ETL is decreased by partially covering the ETL with MGs and the probability of a photogenerated electron recombining or becoming trapped by SnO_2 defects decreases. In our proposed mechanism, partial coverage of the ETL with insulating MGs confers ETL contacts of nanoscale dimensions which are tuneable *via* MG concentration. This passivation mechanism does not depend on MG charge as evidenced by the MG-COOH results discussed above and in Additional Note S1 (ESI†).

Using UV/ozone to decrease blocking of the ETL by the MGs

From the device data (Fig. 2C) and discussion above, it follows that the close-packed MG islands provided too few inter-MG gaps to allow efficient charge transfer to the ETL even with their frequent packing errors (Fig. S13, ESI†). We sought to engineer additional inter-MG gaps within the hexagonally close packed MG islands by controlled etching using UV/ozone (UVO) treatment. The conditions used are detailed in the Experimental details (ESI†). Accordingly, we selected the MG-containing system that gave the best PCE (from Fig. 2C) with the least recombination (as judged by SCLC data) for this purpose, *i.e.*, the 10 mg mL^{-1} PS MG system.

We first investigated the effect of UVO treatment on the MGs. We term the UVO-treated MGs as UVO-MGs. AFM data gave a UVO-MG diameter of ~500 nm and height of ~40 nm

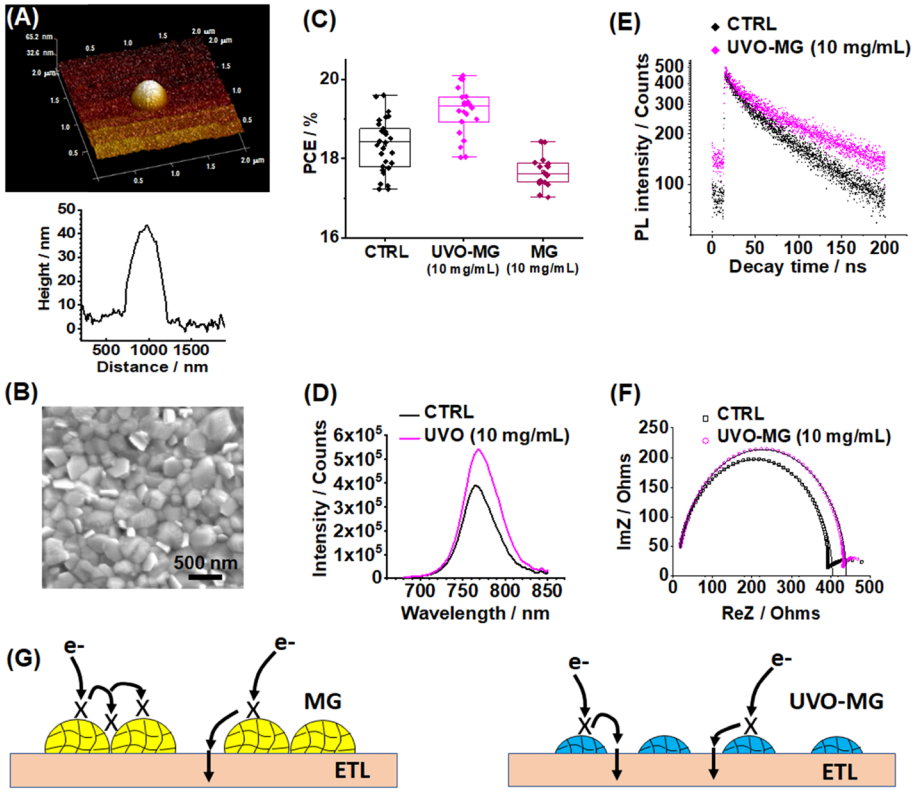

Fig. 4 (A) A 3D AFM image and a line profile for a representative UVO-MG particle. (B) A SEM image of a perovskite film deposited on a glass/ITO/SnO_2/UVO-MG (10 mg mL^{-1}) substrate. (C) Box plots of PCE for selected systems (shown). (D) Steady state PL spectra for the control film and the film shown in (B). (E) TRPL data for the control film and the film shown in (B). (F) EIS data for the films. (G) Proposed mechanism for the improved performance of the UVO-MG system (see text).

(Fig. 4A). SEM data (Fig. S17, ESI†) gave the average diameter of the UVO-MGs to be 521 ± 110 nm. The comparison of these data with those for the pristine MGs (Fig. 2A and B, and S1D (ESI†)) shows that UVO treatment approximately halved the particle diameter and height. Crucially, decreasing the MG diameter produced gaps between adjacent MGs within the formerly close packed MG islands (Fig. S17A, ESI†). The production of inter-MG gaps resulted in smaller blocking distances. The latter distances decreased to the diameter of the UVO-MGs (~500 nm). Furthermore, the coverage of the ETL for the 10 mg mL^{-1} UVO-MG system decreased from 27.5% to 14.3%.

UVO treatment introduced some oxygen groups into the MGs as discussed in Additional Note S2 of the ESI and Fig. S18 and S19 (ESI†). The particles remained positively charged due to the amine groups of the initiator (Fig. S20, ESI†). The combination of decreased coverage and increased oxygen content of the UVO-MGs caused the contact angle for water droplets on the 10 mg mL^{-1} UVO-MG system to decrease to 16.8° (Fig. S21, ESI†). The latter value is larger than the contact angle of 4.3° for the control (glass/ITO/SnO_2) but much smaller than the value of 80.1° for the pristine 10 mg mL^{-1} MG surface (Fig. S4, ESI†). A top-view SEM image shows that the perovskite morphology was unchanged (Fig. 4B) by deposition on the UVO-MGs. The average grain size is 375 ± 73 nm and is not distinguishable from that of the pristine 10 mg mL^{-1} MG system (379 ± 57 nm). The smaller height of the UVO-MGs is evident from cross-sectional SEM image of the perovskite (Fig. S22, ESI†).

Devices were constructed using the 10 mg mL^{-1} UVO-MG system. The highest PCE of 20.09% was recorded for the best device of this system (Fig. S23A and Table S1, ESI†). A Student's *t*-test analysis of the PCE data (Additional Note S3 and Table S4, ESI†) confirms that the average PCE of the UVO-MG system is significantly higher than that for the control. The box plots (Fig. 4C and S23B–E (ESI†)) compared to those for the 10 mg mL^{-1} MG devices and control (Fig. S8, ESI†) show that the improved PCE compared to the control is primarily due to the improved FF and V_{oc}. As shown in Fig. 4C, the average PCE for the 10 mg mL^{-1} UVO-treated MG system is also higher than that for the 10 mg mL^{-1} MG system. The latter conclusion is supported by the results of the Student's *t*-test for these two systems (see also Additional Note S3 and Table S4, ESI†). This is due to the much higher FF for the UVO-MG system (Table S1, ESI†).

The improved performance of the UVO-MG system compared to the control is due to the UVO-MG/perovskite interface preventing recombination. This is supported by the steady state PL data which show a higher PL intensity than the control (Fig. 4D). The data are also consistent with a decrease in quenching compared to the control due to 14.3% of the ETL being covered. The TRPL data (Fig. 4E and Table

S2 (ESI†)) are consistent with these trends of MG-based systems with a slower decay profile and larger τ_{eff} compared to those of the control (Fig. 3C and D). Indeed, the τ_{eff} value for the UVO-MG system is between those of the control and MG system (Table S2, ESI†) as expected based on the coverage by the MGs. EIS data for the UVO-MG system (Fig. 4F) show that the R_p value is 427 Ω which is greater than that of the control (393 Ω) but less than that of the 10 mg mL^{-1} MG system (752 Ω) (Table S3, ESI†). This suggests that passivation was also effective in the UVO-MG system. The R_s value of 12.9 Ω is also less than the pristine 10 mg mL^{-1} MG system (13.8 Ω) due to more inter-MG gaps. An additional contribution to the improved performance of the UVO-MG system may be the reduced MG height.

Space-charge-limited current (SCLC) measurements were performed for the UVO-MG system using an electron only device (Fig. S24, ESI†) and an N_d of 5.5×10^{15} cm^{-3} was calculated. This value is lower than the control system suggesting that passivation occurred. To probe recombination, Suns-V_{oc} and Suns-J_{sc} measurements for the UVO-MG treated system were performed and compared to the control. The V_{oc} data (Fig. S25A, ESI†) were analyzed using[52]

$$n_{id} = \left(\frac{q}{kT}\right)\left(\frac{dV_{oc}}{d\ln I}\right) \quad (4)$$

where n_{id} is the ideality factor. The parameters k, T and I are the Boltzmann constant, temperature and normalized light intensity, respectively. The ideality factor decreases from 1.87 for the control to 1.53 for the UVO-treated MG system. These results show that the UVO-MGs decreased the amount of trap-assisted recombination.[53] The Suns-J_{sc} data (Fig. S25B, ESI†) were analyzed using a power law function[54] ($J_{sc} \sim I^{\alpha}$). The α value increased from 0.937 for the control to 0.965 for the UVO-MG device, which indicates that less bimolecular recombination occurred for the latter.[52]

Based on the above, we suggest that the improved performance for the UVO-MG system compared to the MG systems is because more of the ETL surface is available between MGs for charge transfer to the ETL as a result of UVO treatment (depicted in Fig. 4G) together with passivation of the perovskite by the MGs. The maximum blocking distance with UVO treatment is only ~500 nm; whereas, it can be several micrometers for close-packed MG islands (Fig. S13, ESI†). The former is less than the diffusional distance of charge carriers ~1 μm,[8,46] which results in less recombination and a higher FF which increases the PCE.

Conclusions

In this study, we have investigated the effects of partial coverage of the ETL of n-i-p PSCs on the device performance using PS MGs as well-defined blocking particles. The partial coverage of the ETL was controlled by changing the particle concentration as shown in Fig. 2C. UVO treatment was then used to open additional gaps to the ETL, which decreased coverage. In principle, the UVO treatment should enable fine control of the ETL coverage using treatment time and/or light intensity. Our work involving the pristine MGs provided evidence of passivation of the perovskite by the buried MGs. An unexpected result was that appreciable J_{sc} values were recorded even though the coverage of the ETL was 85.2%. This was ascribed to the gaps between the particles due to packing errors within hexagonally close-packed MG islands. We increased inter-MG gaps using UVO treatment and showed that the device performance improved. This is due to the blocking distance decreasing to ~500 nm which is less than the diffusion length of the charge carriers. The best device of the study (10 mg mL^{-1} UVO-MG), PCE = 20.09%, had an ETL coverage of 14.3%, which implies that not all of the ETL area in planar PSCs is required to achieve maximum PCE. The two hypotheses that underpinned the study are upheld by the results obtained. Overall, this work demonstrates that the ETL of n-i-p PSCs can be decorated with insulating particles with a size ~ wavelength of light and still provide efficient devices or even devices with improved PCE. Our new approach to ETL engineering could lead to enhanced light management if the MGs contained light scatterers or even quantum dots (QDs).[55] Finally, it is worth noting that the PS MG synthesis is scalable to industrial quantities and the approach used here should be applicable to other PSCs.

Author contributions

A. Altujjar synthesized the MGs and characterized them, prepared the perovskite films and characterized them, constructed all the devices and measured their performance characteristics, and assisted with the writing of the manuscript. R. Wang helped with the device construction, obtained the SEM cross sections and conducted the contact angle measurements. X. Wang helped with the MG synthesis. J. M. Saunders conducted the zeta potential measurements and helped with data interpretation. Z. Jia conducted the XRD measurements. B. Spencer conducted the XPS experiments and helped with data interpretation. N. Hodson conducted the AFM measurements and helped with data interpretation. J. Jacobs conducted the EIS measurements. O. M. Alkhudhari conducted the transmission spectral measurements. A. Thomas helped with XPS data interpretation and manuscript writing. R. Curry assisted with manuscript writing. B. R. Saunders conceived the project and led the manuscript writing.

Conflicts of interest

There are no conflicts to declare.

Acknowledgements

The authors thank the EPSRC for funding (EP/R020590/1, EP/X012263/1 and EP/V001914/1). We also thank the Saudi Arabian Cultural Bureau in the UK and Imam Abdulrahman Bin Faisal University for scholarship support (to A. A.). The

authors thank the staff of the EM Core and XRD facilities at The University of Manchester and the Wellcome Trust for equipment grant support to the EM Core Facility.

References

1 R. Azmi, E. Ugur, A. Seitkhan, F. Aljamaan, A. S. Subbiah, J. Liu, G. T. Harrison, M. I. Nugraha, M. K. Eswaran, M. Babics, Y. Chen, F. Xu, T. G. Allen, A. U. Rehman, C.-L. Wang, T. D. Anthopoulos, U. Schwingenschlögl, M. De Bastiani, E. Aydin and S. De Wolf, *Science*, 2022, **376**, 73–77.
2 M. A. Green, A. Ho-Baillie and H. J. Snaith, *Nat. Photonics*, 2014, **8**, 506.
3 N. J. Jeon, J. H. Noh, W. S. Yang, Y. C. Kim, S. Ryu, J. Seo and S. I. Seok, *Nature*, 2015, **517**, 476–480.
4 J. Jeong, M. Kim, J. Seo, H. Lu, P. Ahlawat, A. Mishra, Y. Yang, M. A. Hope, F. T. Eickemeyer, M. Kim, Y. J. Yoon, I. W. Choi, B. P. Darwich, S. J. Choi, Y. Jo, J. H. Lee, B. Walker, S. M. Zakeeruddin, L. Emsley, U. Rothlisberger, A. Hagfeldt, D. S. Kim, M. Grätzel and J. Y. Kim, *Nature*, 2021, **592**, 381–385.
5 H. Min, D. Y. Lee, J. Kim, G. Kim, K. S. Lee, J. Kim, M. J. Paik, Y. K. Kim, K. S. Kim, M. G. Kim, T. J. Shin and S. Il Seok, *Nature*, 2021, **598**, 444–450.
6 A. Miyata, A. Mitioglu, P. Plochocka, O. Portugall, J. T.-W. Wang, S. D. Stranks, H. J. Snaith and R. J. Nicholas, *Nat. Phys.*, 2015, **11**, 582–587.
7 N.-G. Park, *Mater. Today*, 2015, **18**, 65–72.
8 S. D. Stranks, G. E. Eperon, G. Grancini, C. Menelaou, M. J. Alcocer, T. Leijtens, L. M. Herz, A. Petrozza and H. J. Snaith, *Science*, 2013, **342**, 341–344.
9 A. Kojima, K. Teshima, Y. Shirai and T. Miyasaka, *J. Am. Chem. Soc.*, 2009, **131**, 6050–6051.
10 R. A. Belisle, W. H. Nguyen, A. R. Bowring, P. Calado, X. Li, S. J. C. Irvine, M. D. McGehee, P. R. F. Barnes and B. C. O'Regan, *Energy Environ. Sci.*, 2017, **10**, 192–204.
11 Z. Guo, A. K. Jena, G. M. Kim and T. Miyasaka, *Energy Environ. Sci.*, 2022, **15**, 3171–3222.
12 W. Peng, K. Mao, F. Cai, H. Meng, Z. Zhu, T. Li, S. Yuan, Z. Xu, X. Feng, J. Xu, M. D. McGehee and J. Xu, *Science*, 2023, **379**, 683–690.
13 Z. Dai, S. K. Yadavalli, M. Chen, A. Abbaspourtamijani, Y. Qi and N. P. Padture, *Science*, 2021, **372**, 618–622.
14 M. Hao, T. Duan, Z. Ma, M.-G. Ju, J. A. Bennett, T. Liu, P. Guo and Y. Zhou, *Adv. Mater.*, 2023, **35**, 2211155.
15 L. Yang, H. Zhou, Y. Duan, M. Wu, K. He, Y. Li, D. Xu, H. Zou, S. Yang and Z. Fang, *Adv. Mater.*, 2023, 2211545.
16 T. Bu, J. Li, F. Zheng, W. Chen, X. Wen, Z. Ku, Y. Peng, J. Zhong, Y.-B. Cheng and F. Huang, *Nat. Commun.*, 2018, **9**, 1–10.
17 Q. Chen, C. Peng, L. Du, T. Hou, W. Yu, D. Chen, H. Shu, D. Huang, X. Zhou and J. Zhang, *J. Energy Chem.*, 2022, **66**, 250–259.
18 T. Li, Y. Rui, X. Wang, J. Shi, Y. Wang, J. Yang and Q. Zhang, *ACS Appl. Energy Mater.*, 2021, **4**, 7002–7011.
19 X. Sha, J. Sheng, W. Yang, J. Sun, C. Shou, L. Zhang, N. Zhang, Z. Ying, X. Yang, H. Zhao and J. Ye, *J. Mater. Chem. A*, 2023, **11**, 6556–6564.
20 X. Ji, L. Bi, Q. Fu, B. Li, J. Wang, S. Y. Jeong, K. Feng, S. Ma, Q. Liao, F. R. Lin, H. Y. Woo, L. Lu, A. K.-Y. Jen and X. Guo, *Adv. Mater.*, 2023, **35**, 2303665.
21 W. Ke, D. Zhao, C. Xiao, C. Wang, A. J. Cimaroli, C. R. Grice, M. Yang, Z. Li, C.-S. Jiang and M. Al-Jassim, *J. Mater. Chem. A*, 2016, **4**, 14276–14283.
22 H. Wang, F. Li, P. Wang, R. Sun, W. Ma, M. Chen, W. Miao, D. Liu and T. Wang, *Adv. Energy Mater.*, 2020, **10**, 2000615.
23 J. Xie, K. Huang, X. Yu, Z. Yang, K. Xiao, Y. Qiang, X. Zhu, L. Xu, P. Wang and C. Cui, *ACS Nano*, 2017, **11**, 9176–9182.
24 S. Das and V. Jayaraman, *Prog. Mater. Sci.*, 2014, **66**, 112–255.
25 Y. Chen, Q. Wang, Y. Yao, J. Yang, W. Tang, W. Qiu, Y. Wu and Q. Peng, *Energy Environ. Sci.*, 2023, **16**, 5243–5254.
26 K. Liu, S. Chen, J. Wu, H. Zhang, M. Qin, X. Lu, Y. Tu, Q. Meng and X. Zhan, *Energy Environ. Sci.*, 2018, **11**, 3463–3471.
27 Z. Xiong, X. Chen, B. Zhang, G. O. Odunmbaku, Z. Ou, B. Guo, K. Yang, Z. Kan, S. Lu, S. Chen, N. A. N. Ouedraogo, Y. Cho, C. Yang, J. Chen and K. Sun, *Adv. Mater.*, 2022, **34**, 2106118.
28 J. Zhuang, P. Mao, Y. Luan, N. Chen, X. Cao, G. Niu, F. Jia, F. Wang, S. Cao and J. Wang, *Adv. Funct. Mater.*, 2021, **31**, 2010385.
29 J. Peng, D. Walter, Y. Ren, M. Tebyetekerwa, Y. Wu, T. Duong, Q. Lin, J. Li, T. Lu, M. A. Mahmud, O. L. C. Lem, S. Zhao, W. Liu, Y. Liu, H. Shen, L. Li, F. Kremer, H. T. Nguyen, D.-Y. Choi, K. J. Weber, K. R. Catchpole and T. P. White, *Science*, 2021, **371**, 390–395.
30 B. R. Saunders and B. Vincent, *Adv. Colloid Interface Sci.*, 1999, **80**, 1–25.
31 J. H. Heo, M. H. Jang, M. H. Lee, H. J. Han, M. G. Kang, M. L. Lee and S. H. Im, *J. Mater. Chem. A*, 2016, **4**, 16324–16329.
32 T. Wang, Z. Cheng, Y. Zhou, H. Liu and W. Shen, *J. Mater. Chem. A*, 2019, **7**, 21730–21739.
33 J. Wu, Y. Cui, B. Yu, K. Liu, Y. Li, H. Li, J. Shi, H. Wu, Y. Luo and D. Li, *Adv. Funct. Mater.*, 2019, **29**, 1905336.
34 J. Kong, H. Wang, J. A. Röhr, Z. S. Fishman, Y. Zhou, M. Li, M. Cotlet, G. Kim, C. Karpovich, F. Antonio, N. P. Padture and A. D. Taylor, *ACS Appl. Energy Mater.*, 2020, **3**, 7231–7238.
35 M. Li, X. Yan, Z. Kang, Y. Huan, Y. Li, R. Zhang and Y. Zhang, *ACS Appl. Mater. Interfaces*, 2018, **10**, 18787–18795.
36 J. Ran, P. Yuan, H. Xie, F. Wan, Y. Chen, Y. Yuan, M. He, J. Li, X. Wang, A. Pan, Y. Gao and B. Yang, *Sol. RRL*, 2020, **4**, 2000490.
37 X. Wen, J. Wu, D. Gao and C. Lin, *J. Mater. Chem. A*, 2016, **4**, 13482–13487.
38 H. Zhang, J. Shi, L. Zhu, Y. Luo, D. Li, H. Wu and Q. Meng, *Nano Energy*, 2018, **43**, 383–392.
39 R. K. Gupta, R. Garai and P. K. Iyer, *ACS Appl. Energy Mater.*, 2021, **4**, 10025–10032.
40 A. Altujjar, M. Z. Mokhtar, Q. Chen, J. Neilson, B. F. Spencer, A. Thomas, J. M. Saunders, R. Wang, O. Alkhudhari and A. Mironov, *ACS Appl. Mater. Interfaces*, 2021, **13**, 58640–58651.

41 C. Dokkhan, M. Z. Mokhtar, C.-R. Ke, A. S. Walton, Q. Chen, N. W. Hodson, Q. Lian and B. R. Saunders, *ACS Appl. Energy Mater.*, 2019, **2**, 6624–6633.
42 Q. Lian, M. Z. Mokhtar, D. Lu, M. Zhu, J. Jacobs, A. B. Foster, A. G. Thomas, B. F. Spencer, S. Wu and C. Liu, *ACS Appl. Mater. Interfaces*, 2020, **12**, 18578–18589.
43 M. Chen, M. Z. Mokhtar, E. Whittaker, Q. Lian, B. Hamilton, P. O'Brien, M. Zhu, Z. Cui, S. A. Haque and B. R. Saunders, *Nanoscale*, 2017, **9**, 10126–10137.
44 S. Schmidt, H. Motschmann, T. Hellweg and R. von Klitzing, *Polymer*, 2008, **49**, 749–756.
45 H. Min, M. Kim, S.-U. Lee, H. Kim, G. Kim, K. Choi, J. H. Lee and S. I. Seok, *Science*, 2019, **366**, 749–753.
46 P. Li, Y. Zhang, C. Liang, G. Xing, X. Liu, F. Li, X. Liu, X. Hu, G. Shao and Y. Song, *Adv. Mater.*, 2018, **30**, 1805323.
47 P. Caprioglio, F. Zu, C. M. Wolff, J. A. Márquez Prieto, M. Stolterfoht, P. Becker, N. Koch, T. Unold, B. Rech, S. Albrecht and D. Neher, *Sustainable Energy Fuels*, 2019, **3**, 550–563.
48 D. Shi, V. Adinolfi, R. Comin, M. Yuan, E. Alarousu, A. Buin, Y. Chen, S. Hoogland, A. Rothenberger, K. Katsiev, Y. Losovyj, X. Zhang, P. A. Dowben, O. F. Mohammed, E. H. Sargent and O. M. Bakr, *Science*, 2015, **347**, 519–522.
49 V. Gonzalez-Pedro, E. J. Juarez-Perez, W.-S. Arsyad, E. M. Barea, F. Fabregat-Santiago, I. Mora-Sero and J. Bisquert, *Nano Lett.*, 2014, **14**, 888–893.
50 Z. Li, P. P. Boix, G. Xing, K. Fu, S. A. Kulkarni, S. K. Batabyal, W. Xu, A. Cao, T. C. Sum and N. Mathews, *Nanoscale*, 2016, **8**, 6352–6360.
51 E. Franklin, K. Fong, K. McIntosh, A. Fell, A. Blakers, T. Kho, D. Walter, D. Wang, N. Zin, M. Stocks, E.-C. Wang, N. Grant, Y. Wan, Y. Yang, X. Zhang, Z. Feng and P. J. Verlinden, *Progr. Photovolt.: Res. Appl.*, 2016, **24**, 411–427.
52 D. Glowienka and Y. Galagan, *Adv. Mater.*, 2022, **34**, 2105920.
53 T. Liu, J. Guo, D. Lu, Z. Xu, Q. Fu, N. Zheng, Z. Xie, X. Wan, X. Zhang and Y. Liu, *ACS Nano*, 2021, **15**, 7811–7820.
54 T. Singh, M. Ikegami and T. Miyasaka, *ACS Appl. Energy Mater.*, 2018, **1**, 6741–6747.
55 M. Bradley, N. Bruno and B. Vincent, *Langmuir*, 2005, **21**, 2750–2753.